Nanoscale

PAPER

Cite this: *Nanoscale*, 2024, **16**, 12599

Insight into the transport of ions from salts of moderated solubility through nanochannels: negative incremental resistance assisted by geometry†

Gregorio Laucirica, *‡[a] L. Miguel Hernández Parra, [a] Angel L. Huamani, [a] Michael F. Wagner,[b] Alberto G. Albesa,[a] María Eugenia Toimil-Molares, [b,c] Waldemar Marmisollé *[a] and Omar Azzaroni *[a]

In this study, the transport of salt with moderate solubility through bioinspired solid-state nanochannels was comprehensively investigated. For this purpose, bullet-shaped channels were fabricated and exposed to $KClO_4$, a monovalent salt with moderate solubility. These channels displayed the typical rectifying behavior characteristic of asymmetrical channels but with one remarkable difference, the iontronic output exhibited a negative incremental resistance phenomenon of high gating efficiency when the transmembrane voltage in the open state was increased enough, giving rise to an inactivated state characterized by a low and stable ion current. The behavior is attributed to salt precipitation inside the channel and remarkably, it is not observed in other geometries such as cylindrical or cigar-shaped channels. Considering the central role of the surface in precipitation formation, the influence of several parameters such as electrolyte concentration, pH, and channel size was studied. Under optimized conditions, this system can alternate among three different conductance states (closed, open, and inactivated) and exhibits gating ratios higher than 20. Beyond its potential application in fields related to electronics or sensing, this study provides valuable insight into the fundamental principles behind ion rectifying behavior in solid-state channels and highlights the implications of surface phenomena at the nanoscale.

Received 5th December 2023,
Accepted 17th May 2024

DOI: 10.1039/d3nr06212k

rsc.li/nanoscale

Introduction

Biological ion channels are proteins embedded in cell membranes that facilitate the transport of ions beyond the cell boundaries, playing a central role in several physiological functions of organisms.[1,2] The remarkable control and sophistication in ion transport achieved by this kind of system have positioned it as an inspiring model for the development of synthetic nanofluidic membranes. As a result, understanding and studying ion transport through solid-state nanochannels (SSNs) have gained considerable interest in the last few decades.[3,4] In particular, fully abiotic membranes with analog properties to ion channels have shown promising results for the development of platforms with applications in different fields such as nanofluidic chemical actuation,[5,6] sensing,[7–9] nanoelectronic,[10–12] and energy conversion.[13–16]

The combination of charged surfaces and nanometric channel structures gives rise to several new phenomena not observed in the micrometric scale due to the decrease in scale to the characteristic range of electrostatic interactions.[4,17,18] In the case of nanometric channels, the interplay between channel geometry and surface properties determines the ion transport properties through the nanostructure. These transport properties are typically studied by recording the ion current at different transmembrane voltages, which produces an iontronic output.

One of the most intriguing properties of these bioinspired channels is the possibility of generating iontronic signals similar to those obtained with some electrical components, such as resistors and diodes. Disruption of the symmetry in the electrical potential profile, for instance, gives rise to rectifying behavior, where the current is favored in a specific transmembrane voltage polarity.[19] Similar to their biological

[a]*Instituto de Investigaciones Fisicoquímicas Teóricas y Aplicadas (INIFTA), Departamento de Química, Facultad de Ciencias Exactas, Universidad Nacional de La Plata, CONICET, CC 16 Suc. 4, La Plata B1904DPI, Argentina. E-mail: gregoriolaucirica@quimica.unlp.edu.ar, wmarmi@inifta.unlp.edu.ar, omarazzaroni@quimica.unlp.edu.ar*

[b]*GSI Helmholtzzentrum für Schwerionenforschung, 64291 Darmstadt, Germany*

[c]*Technische Universität Darmstadt, Materialwissenschaft, 64287 Darmstadt, Germany*

†Electronic supplementary information (ESI) available. See DOI: https://doi.org/10.1039/d3nr06212k

‡Current affiliation: UCAM-SENS, Universidad Católica San Antonio de Murcia, UCAM HiTech, 30107 Murcia, Spain.

counterpart, such systems exhibit open (high ion flux) and closed (low ion flux) conductance states depending on the transmembrane voltage polarity. Recently, it has been demonstrated that rectifying systems can also display a negative incremental resistance (NIR) phenomenon with a high gating ratio.[20] The NIR phenomenon, also known as negative differential resistance, refers to a sudden decrease in current when voltage is increased beyond a certain point. It has been observed in different devices such as nanochannels, microchannels, and elastomeric membranes.[21–24] Additionally, various solid-state electronic devices like transistors or junctions also exhibit this behavior.[25–27] NIR-based transport has attracted significant interest due to its potential application in memories, switches, high-frequency oscillators, and functional circuits.[25,28,29]

The appearance of this peculiar non-ohmic behavior in the iontronic output displayed by SSNs has been reported under different conditions. For instance, NIR events have been evidenced by recording current–voltage (*I–V*) curves with multivalent ions[21,30–33] or fluoride[20] in solution, and under concentration or viscosity gradients combined with external pressure forces[24,34] or nonlinear electrokinetic effects.[23,35] In all the cases, the effects arising from the surface charges in the channel or membrane have been highlighted as one of the main factors. Based on the dependence of the surface charge and the NIR phenomenon, several authors have proposed and demonstrated that this kind of system can be useful in the development of nanofluidic sensors, in addition to the abovementioned electronic applications.[20,23,24]

Among the different mechanisms to evidence the NIR event in the iontronic output, the use of multivalent salts with low solubility represents an interesting alternative. Previous reports from Siwy's group have shown that the use of conical channels exhibiting ion current rectification can display NIR events due to the salt precipitation inside narrow channels (sub-10 nm tip diameters) due to the concentration polarization.[21,30] In these works, the authors found that the *I–V* curves recorded in the presence of low soluble salts (in concentrations below its solubility limit), including $CaHPO_4$, $CoHPO_4$, Mg(OH), *etc.*, give rise to NIR events accompanied with strong current instabilities. They attributed the salt precipitation to the ion enrichment inside conical channels induced by the presence of surface charge and the application of a certain magnitude of transmembrane voltage (V_t). For this, alkaline pH conditions and narrow tip channel diameters were highlighted as requirements because such conditions accentuate the surface charge effects on ion transport. While these articles provided the foundations of the presence of NIR phenomena in the iontronic outputs due to precipitation and some keys regarding the influence of different parameters, most of the attention was focused on the current oscillations. In particular, considerable efforts have been devoted to understand the origin, modulate the frequency, and apply such instabilities.[31,32,36–38]

This article analyzes ion transport through SSNs of different geometries and sizes in the presence of $KClO_4$, a monovalent salt of moderated solubility. In particular, bullet-shaped channels exposed to $KClO_4$ display a typical rectifying behavior but with one unique difference: if the transmembrane voltage in the open state is increased enough, the iontronic output exhibits a NIR phenomenon. The behavior is attributed to salt precipitation inside the channel but, in contrast to the reported behavior of conical channels in the presence of $CaHPO_4$ or $CoHPO_4$, the NIR event is accompanied by a low and stable ion current state that was referred to as inactivated state. Analogously to the biological channel, the single bullet-shaped nanochannels demonstrate the existence of three different ion transport states (close, open, and inactivated) that can be easily tuned by modulating the magnitude and polarity of V_t. This trend was not evidenced in other geometries such as cylindrical or cigar-shaped channels, *i.e.* it is favored by the asymmetric geometry. Remarkably, the characteristics and efficiency of the NIR phenomenon are also sensitive to other properties of the channel such as the surface charge density and size. In contrast to the previous works available in the literature, our systematic study illustrates how the interplay between channel dimensions, electrolyte nature, and concentration allows obtaining not only the NIR effect but also a very stable iontronic signal with three different states. Therefore, we introduce the use of salt nanoprecipitation not only to obtain iontronic outputs with highly efficient NIR phenomenon but also the development of a nanofluidic device with three different and stable transport states.

Beyond the peculiar iontronic output and the high gating ratio displayed by the system, the measurements under these conditions provide an invaluable source of information to experimentally elucidate the fundamental principles behind the ion rectifying behavior in solid-state channels. In addition, supported by Poisson–Nernst–Planck (PNP) simulations, the article includes a comprehensive study of the influence of the experimental conditions (electrolyte concentration, pH, channel geometry, tip diameter, *etc.*) which enables a deeper insight into the occurrence of precipitation in charged channels. This example highlights the incidence of surface phenomena at the nanoscale and the possibility of studying them by recording the iontronic signal.

Materials and methods

Nanochannel fabrication

SSNs of different geometries were created on polyethylene terephthalate (PET) membranes by the ion-track-etching technology.[39] PET foils of 12 μm of thickness were irradiated with swift heavy ions with an energy of 11.4 MeV per nucleon. Ion transport experiments were performed in single-channel membranes, *i.e.* irradiated with a single swift heavy ion, whereas scanning electron microscopy characterizations were performed in multi-channel membranes, *i.e.* irradiated with 10^6 ions per cm^2. The etching protocol was varied in order to obtain channels with different geometries.

Bullet-shaped nanochannels were obtained through a surfactant-assisted protocol in which the membrane was previously exposed to UV light for 24 hours and then soaked in a solution of 6 M NaOH + 0.05% w/w Dowfax 2a1 surfactant at 60 °C. The etching time was 6 minutes unless otherwise stated. The bullet-shaped geometry contains a narrow aperture with a parabolic profile (tip) and a wide aperture with a cylindrical profile (base) (SEM characterization available in ESI, section 1†).

For the cigar-shaped nanochannel, the etching protocol involved immersing the irradiated PET membrane in a solution of 6 M NaOH + 0.05% w/w Dowfax 2a1 surfactant at 60 °C for 6 minutes. In contrast to the bullet-shaped geometry, the cigar-shaped geometry contains narrow apertures with a parabolic profile (tips) at both membrane sides (SEM characterization available in ESI, section 1†).

The cylindrical nanochannel was obtained by soaking the irradiated membrane in 2 M NaOH at 50 °C for 6 minutes. The size analysis was performed by conductimetric measurements at 1 M and 3 M of KCl (see ref. 13 for further details).

Iontronic measurements

For the ion transport experiments, single-nanochannel membranes were placed in a custom cell separating two half-cells filled with a supporting electrolyte.[13] A four-electrode arrangement consisting of two Ag/AgCl electrodes and two platinum wires was connected to a potentiostat, allowing the control of the transmembrane voltage and the current recording. The working electrode and its Ag/AgCl reference electrode were placed in the reservoir facing the channel tip, whereas the counter-electrode and its Ag/AgCl reference electrode were in the reservoir facing the channel base. Current–voltage (*I–V*) curves were recorded with a scan rate of 100 mV s^{-1} and in 0.1 M $KClO_4$ unless otherwise specified. The pH condition was set at pH = 3.5, pH = 6, or pH = 9 by adding small amounts of $HClO_4$ or KOH, accordingly.

Rectification factor (f_{rec}), NIR ratio, and voltage threshold

The results were analyzed in terms of the rectification factor, NIR ratio, and voltage threshold. The rectification factor constitutes a measurement of the rectification efficiency and is calculated with the following equation:[40]

$$\begin{cases} f_{rec} = -\dfrac{|I(+3\,V)|}{|I(-3\,V)|} & < 0 \text{ when } I(+3\,V) > |I(-3\,V)| \\ f_{rec} = \dfrac{|I(-3\,V)|}{|I(+3\,V)|} & > 0 \text{ when } |I(+3\,V)| | I(-3\,V)| \end{cases} \quad (1)$$

For its part, the NIR ratio was calculated as the ratio between the maximum current (I_{max}) in the high conductance branch (open branch) and the current at +3 V:

$$\text{NIR ratio} = \frac{I_{max}}{I(+3\,V)} \quad (2)$$

Finally, the voltage threshold (V_{thres}) was determined as the V_t magnitude where the current takes its maximum value (I_{max}) or, in other words, the V_t value in the open branch just before the NIR event.

Results and discussion

The iontronic output of a single PET bullet-shaped nanochannel in aqueous soluble salts like 0.1 M KCl exhibits a rectifying behavior at pH > 3 (Fig. 1(a)). This particular iontronic behavior has been extensively reported and explained in different nanochannel systems.[41–43] In this regard, the *I–V* curve recorded in 0.1 M KCl pH 9 displays a high and low conductance branch at positive and negative V_t respectively. This trend is typically attributed to an accumulation/depletion mechanism promoted by the interaction between surface charges and mobile ions, especially in the tip region. At positive V_t, the high conductance branch results from a high accumulation of ions, whereas at negative transmembrane voltages, ions are mostly depleted from the channel. While the fixed surface charge mainly promotes the accumulation of counterions (ions with the opposite charge compared to the surface charge polarity), concentration profiles obtained by PNP models have shown that both kinds of ions are enriched in the high conductance branch (PNP-based results are available in ESI, section 6†).[44] On the contrary, in the low conductance branch, the current is largely explained by counterion transport (selective branch).

When the response is evaluated in a relatively insoluble salt in water like $KClO_4$ (solubility 20 °C ~1.67 g/100 mL ~0.12 M)[45] with a concentration of 0.1 M and adjusted at pH = 9 (see below the pH influence), the iontronic output exhibits an anomalous behavior (Fig. 1(b)). The forward current (from −3 V to +3 V) shows an increase in the current until a limit value of transmembrane voltage (hereinafter, such voltage limit value will be referred to as voltage threshold V_{thres}) where a sharp decrease in the current is produced. As was mentioned, this trend, which constitutes a large deviation from the typical rectifying behavior, has been previously defined as NIR or negative differential resistance.[27–29] If the *I–V* curve is recorded for different cycles (between ±3 V), the trend is maintained. However, as the number of cycles increases, V_{thres} diminishes. Furthermore, it is noteworthy that conducting the *I–V* curve in KCl (with a solubility[45] of approximately 25.39 g/100 mL ~3.40 M at 20 °C) or $NaClO_4$ (with a solubility[45] of approximately 66.2 g/100 mL ~5.41 M at 20 °C) results in a response that exhibits the typical diode-like behavior without NIR events. This observation suggests that the presence of both K^+ and ClO_4^- ions is necessary to evidence the NIR response (see ESI, section 2, Fig. S3†).

Considering the moderated solubility of the $KClO_4$ salt and the ion current rectification behavior of the bullet-shaped nanochannels, a similar line of thinking that those employed by Siwy and coworkers could be applicable here.[21] At high V_t, the salt concentration inside the channel is drastically increased due to the surface charges to an extent that exceeds the concentration given by the bulk solubility product constant

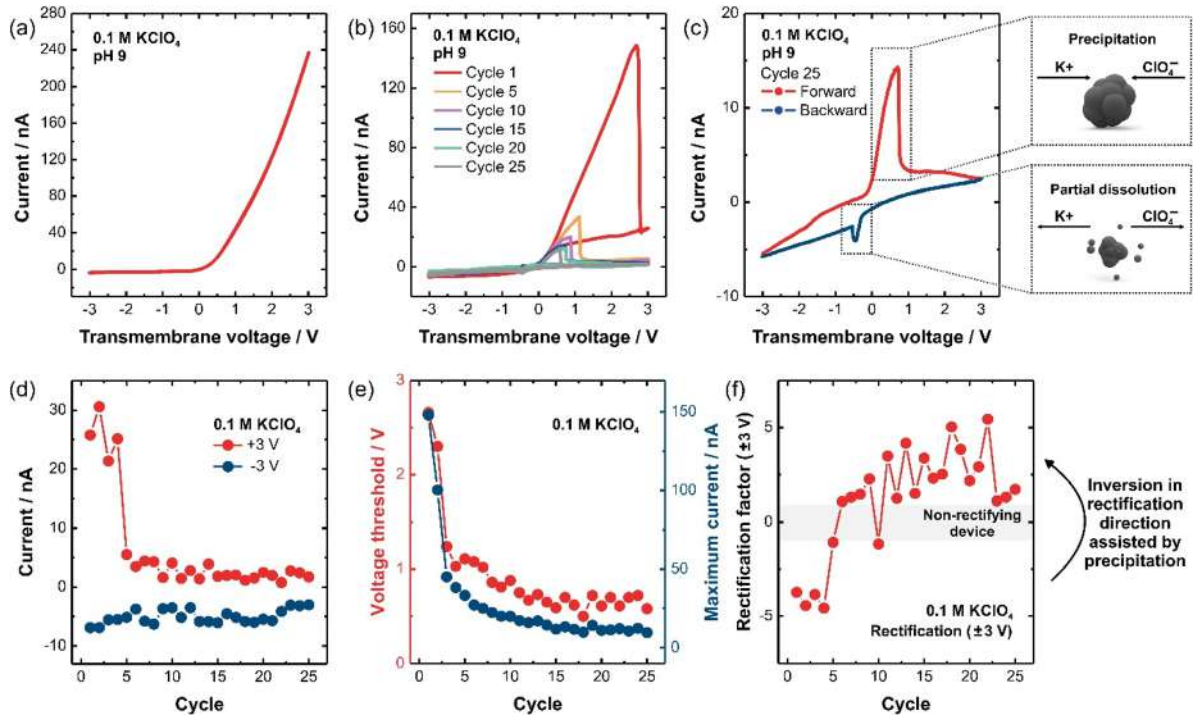

Fig. 1 (a) *I–V* curve recorded in 0.1 M KCl. (b) *I–V* curves recorded in 0.1 M $KClO_4$ during 25 cycles. (c) *I–V* curve obtained for the 25th cycle. (d) Current values obtained in $KClO_4$ at ±3 V for the different cycles. (e) Voltage threshold and maximum current (I_{max}) values obtained in $KClO_4$ for the different cycles. (f) Rectification factor values obtained in $KClO_4$ at ±3 V for the different cycles. All the curves were obtained at pH = 9.

(K_{sp} (25 °C) = 1.05×10^{-2})[45] triggering the salt precipitation inside of the channel. The formation of precipitates promotes the channel blockade that is transduced into an abrupt diminution of the current in the *I–V* curve. To reinforce this hypothesis, the ion distribution at various V_t for a bullet-shaped channel is illustrated in Fig. S9.† In this figure, a noticeable increase in the concentration of both cations and anions can be observed at $V_t > 0$ V, with cations exhibiting a higher degree of enrichment due to the cation-selectivity of pristine PET. This increase in ion concentration within the nanostructure, coupled with the relatively low solubility of the supporting electrolyte, could account for the experimental results.

To clarify this point, Fig. 1(c) shows the *I–V* curve for the channel in the presence of 0.1 M $KClO_4$ after 20 cycles. From V_t = 0 V to 0.7 V, the forward scanning evidences an increase in the current values reaching ~15 nA; however, a sharp decrease in the current to values around ~2 nA is produced when V_t is further increased from 0.7 V to 3 V which constitutes a typical case of NIR event promoted by salt precipitation. In the backward scanning, the curve shows a little peak around $V_t = -0.5$ V (this peak was systematically repeated in all the cycles in different samples). To our best knowledge, the presence of this peak has not been previously reported. It could be likely related to a partial dissolution of the solid since, at negative V_t, the ion concentration is depleted inside the nanofluidic device, which may trigger the dissolution (at least, partially) of the solid (Fig. S9†). Thus, ions released from the solid are rapidly drained, producing a small pulse in the current (in module) which is transduced as a small peak placed at ~−0.5 V in the *I–V* curve.

To gain insight into the ion transport through the channel exposed to the relatively low-soluble salt $KClO_4$, different parameters extracted from the *I–V* curves were analyzed. As shown in Fig. 1(b), the increment in the number of cycles generates a diminution in the current at 3 V due to, presumably, the formation of $KClO_4$ nanoprecipitates (Fig. 1(d)). Specifically, the current at +3 V rapidly diminishes as the cycle number increases and finally, it reaches a constant value around ~2 nA. On the other hand, the current values at −3 V exhibit a diminution (in module) from −6.9 nA to −3 nA. In both cases, the decrease in the current is ascribed to the decrease of inner space due to the precipitation of $KClO_4$. Moreover, V_{thres} decreases as the number of cycles increases (Fig. 1(e)). We hypothesize that the precipitate is not completely dissolved during the backward scan, given that the current change and instability observed during the precipitation event in the forward scan were much greater than those obtained for the dissolution step in the backward scan. Additionally, the presence of solid particles remaining after the precipitation event reduces the amount of salt required to produce the following NIR event explaining why V_{thres} and I_{max} decrease as the cycle number increases. Also, these remaining particles could act as nucleation points in subsequent cycles, facilitating the growth of precipitate leading to further diminution of the voltage required for the NIR event as the number of cycles increases.

The ion current rectification obtained in 0.1 M KCl presents an efficiency highly dependent on several parameters such as ionic strength, transmembrane voltage, the surface charge, and geometry of the channel while the direction of rectification is typically commanded by the polarity of the surface charge. However, in moderated-soluble salts such as $KClO_4$, the appearance of nanoprecipitates triggers anomalous effects in the rectifying behavior. In the present study, an inversion in the rectification direction (evaluated at ±3 V) is evidenced due to the presence of solid particles (Fig. 1(e)). Therefore, while an ON state is expected at positive transmembrane voltages, the accumulation of K^+ and ClO_4^- promotes the crystallization of $KClO_4$ and, subsequent diminution of the current due to the partial occlusion of the pore.

Beyond the involved physical chemistry considerations in the experiments and in contrast to previous reports, it is worth mentioning that the iontronic signal presented in Fig. 1(b) demonstrates three stable distinct regimes.[21,30] Drawing an analogy with biological ion channels, voltage-responsive ion channels have different closed and open states depending on membrane potential.[2,46] In the closed state, the ion flux is impeded, while in the open state, a conformational change in the protein induced by the variation in membrane potential (stimulus) triggers the opening of the channel and allows for ion transport through the cell boundaries. Furthermore, voltage-gated ion channels also present inactivated states where the channel is closed differently even when the activating stimulus is still present.[47–49]

In the system discussed here, while the phenomena involved are distinct compared to the biological case, it is possible to draw a parallelism because ion transport transitions among several similar states (Scheme 1). Under negative transmembrane voltages, the ion flux is in a low state (closed), characteristic of the rectifying behavior of asymmetrical channels (left panel). At low and moderate positive transmembrane voltages, the ion flux is favored (open) and the conductance takes maximum values, also typical of the rectifying behavior of asymmetrical channels (central panel). However, in contrast to a typical rectifying regime, further increases in transmembrane voltage disrupt the high conductance branch by promoting a negative differential resistance and it gives rise to another stable regime of low ion flux (right panel). This state resembles the inactivation of ion channels since although the V_t presents an opening magnitude (*i.e.* positive polarity) the system transitions to a state where the ion flux is drastically unfavored.

To gain insight into the effect of the surface charges in the salt precipitation, K^+ and ClO_4^- transport was studied under different pH conditions and channel sizes (Fig. 2 and 3). The selection of these two variables stems from their appreciable influence on the ion enrichment degree inside the channel. In addition, experiments were also conducted at different electrolyte conditions (further details in ESI, section 3, Fig. S4†). Regarding this, experiments conducted in 0.01 M $KClO_4$ also evidenced the NIR phenomenon but with strong current oscillation. For its part, the iontronic output in 0.001 M $KClO_4$ did not display any NIR event. Considering the higher stability of the signal, the rest of the analysis will be centered on the iontronic output obtained in 0.1 M $KClO_4$.

The *I*–*V* curves of $KClO_4$ at pH values of 3.5, 6, and 9 show that negative incremental resistance events are only evidenced at pH 6 and 9, where the channel surface is appreciably charged (Fig. 2(a)–(c), further details in ESI, section 4, Fig. S5†). On the contrary, at acidic pH, where a relatively low amount of the carboxyl groups is unprotonated and therefore, the surface charge is low, the signal remains invariant for 20 cycles. These results support the main hypothesis related to the precipitation due to the enrichment of counter and co-ions during the rectifying behavior to concentration values reaching the salt solubility limit.

To further analyze the behavior at different pH values, different parameters were studied from the *I*–*V* curves. For instance, Fig. 2(d) shows the current obtained at +3 V in terms of the voltammetry cycles. For the measurements carried out

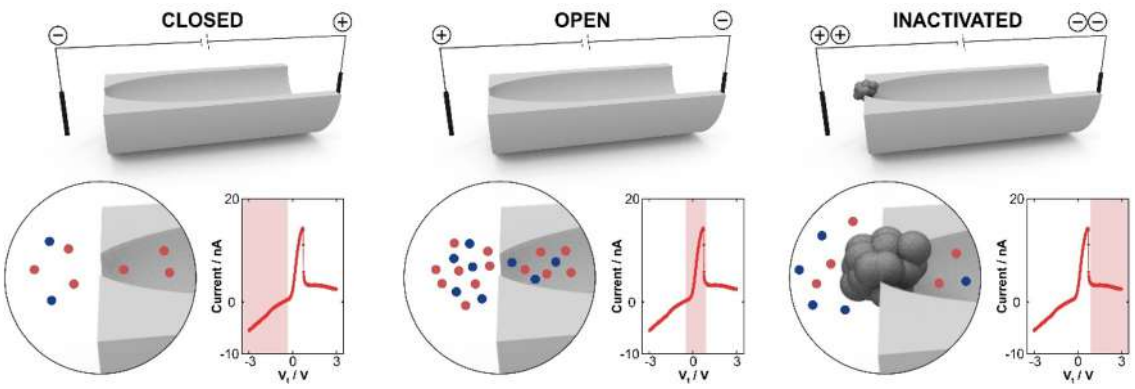

Scheme 1 Illustration of the analogy between this fully abiotic system and the different conductance states of a voltage-gated biological ion channel. The application of a certain transmembrane voltage polarity and magnitude enables modulating the conductance state among closed, open, and inactivated states. In order to construct the analogy with the biological case, a ball-and-chain model was employed to illustrate the inactivated state caused by salt precipitation.

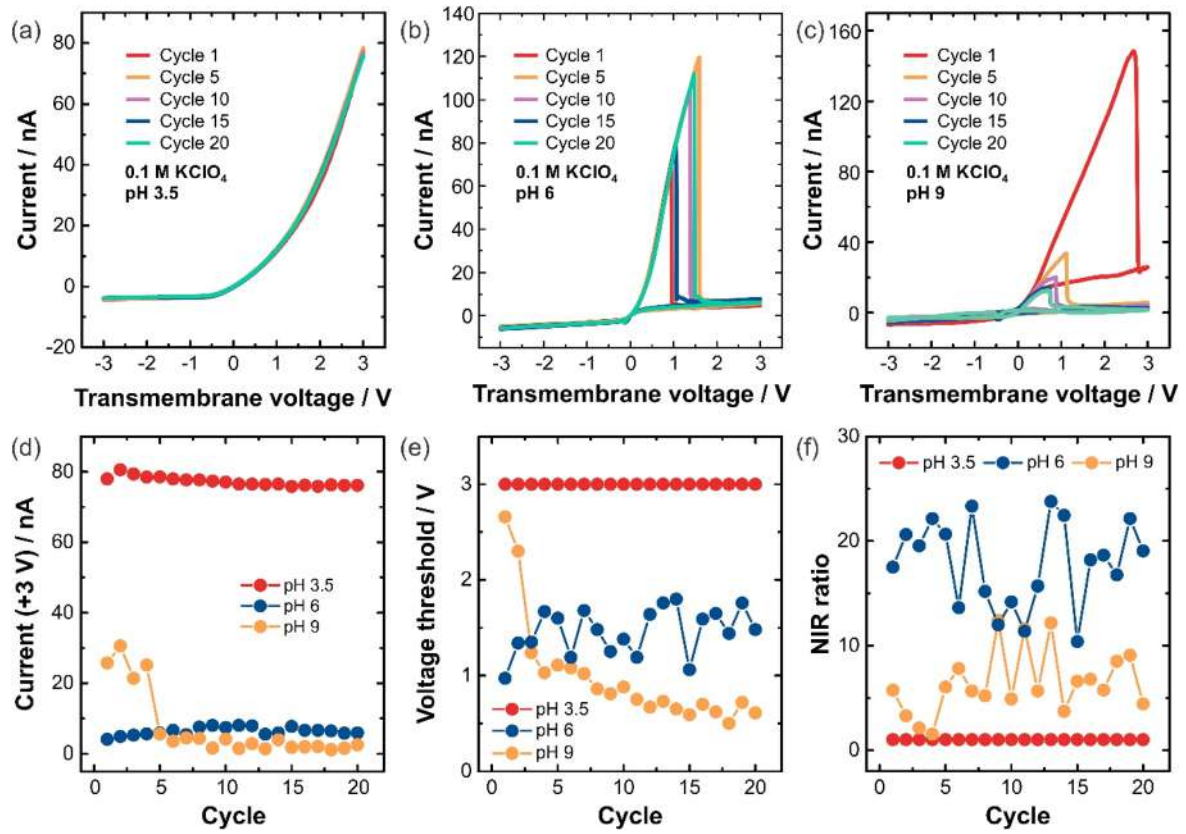

Fig. 2 *I–V* curves recorded in 0.1 M $KClO_4$ at pH values of (a) 3.5, (b) 6, and (c) 9. (d) Current values obtained in $KClO_4$ at ±3 V for the different cycles in the three pH conditions. (e) Voltage threshold obtained in $KClO_4$ for the different cycles. (f) NIR ratio values obtained in $KClO_4$ for the different cycles in the three pH conditions.

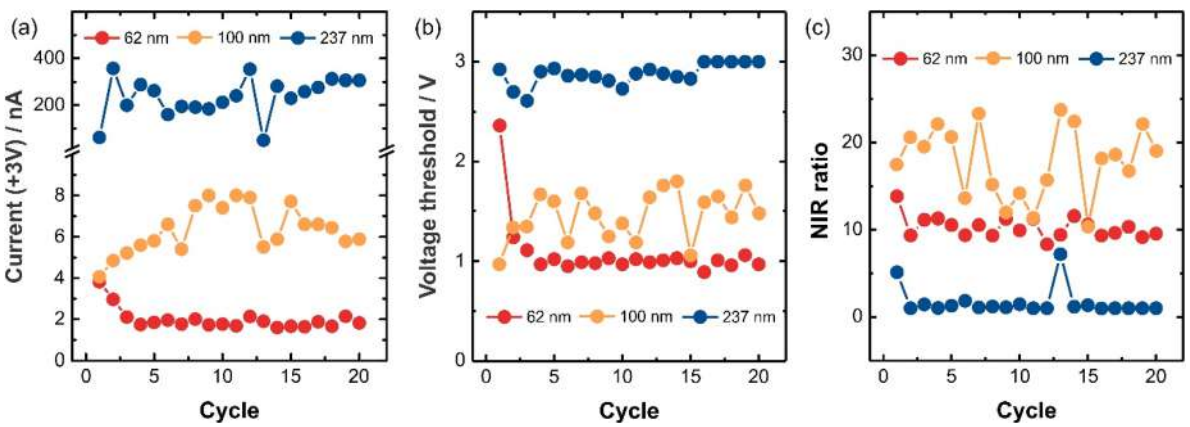

Fig. 3 (a) Current values obtained in $KClO_4$ at ±3 V for the different cycles for the three bullet-shaped channels. (b) Voltage threshold obtained in $KClO_4$ for the different cycles for the three bullet-shaped channels. (c) NIR ratio values obtained in $KClO_4$ for the different cycles for the three bullet-shaped channels. In all the cases, the results were obtained by employing 0.1 M $KClO_4$ at pH 6 as the supporting electrolyte. In all the cases, 62 nm (red), 100 nm (orange), and 237 nm (blue) refer to the tip diameters of the different bullet-shaped channels. The base sizes of each channel can be found in Table 1.

at pH 3.5, the currents at +3 V remain almost invariable for all the cycles with values around of 80 nA, which can be attributed to the absence of precipitation. Conversely, at pH 6 and 9, the current values at +3 V take low magnitudes, due to the probable decrease of the inner space caused by the salt precipitation. This trend is more marked for the alkaline condition, due to the higher surface charge. An analogous analysis can be done by analyzing V_{thres} (Fig. 2(e)). For the case of the measure-

ment at acidic pH, V_{thres} agrees with the maximum transmembrane voltage of +3 V because NIR events are not produced. *I–V* curves at pH 6 and 9 display V_{thres} values <3 V for most of the cycles. In particular, the V_{thres} at pH 9 takes values lower than pH 6 indicating that a lower V_t is needed to promote the NIR phenomenon as the surface acquires a higher charged state.

Considering that in all cases the NIR event involves an abrupt diminution in the current in a small range of voltage, such behavior has been related as a promising property in, for example, sensing applications.[23,24] Given this context, it is interesting to determine the NIR ratio (eqn (2)), *i.e.* the ratio between I_{max} and the current at the maximum V_t, +3 V, because such magnitude gives an idea of the change ratio (sensitivity) (Fig. 2(f)). At acidic pH, where the NIR event is absent in the voltage window ±3 V, the NIR ratio is maintained at 1. However, the NIR ratio takes values higher than 1 for pH 6 and 9. Specifically, the NIR ratio evidences a value of 18 ± 4 (average ± standard deviation) at pH 6, whereas this parameter is around 6.5 ± 3 at pH 9. In particular, the higher I_{max} exhibited at pH 6 explains the increment in the NIR ratio at such conditions. These results indicate that to maximize the NIR ratio, it is not the best option to work at the condition where the salt precipitation is more favorable but instead, intermediate conditions where the relationship of I_{max} and pore blockage is maximized produce higher NIR ratios. This enhancement of the signal related to the NIR phenomenon (the NIR ratio) could be important facing any possible application in different fields such as sensing or nanoelectronics. However, higher NIR ratios come at the expense of increased cycle-to-cycle variability and the necessity of more cycles to reach a steady-state behavior, as shown in Fig. 2(e) and (f). This trend can be attributed to the fact that, at pH 6 where the surface charge is not very high, V_{thres} values are higher and exhibit greater variability, leading to significant fluctuations in I_{max} and, consequently, NIR ratio. Additionally, other samples fabricated and measured under the same conditions have demonstrated similar variability and a greater challenge in attaining steady-state conditions compared to the alkaline condition. In this regard, the ESI† file includes data on V_{thre} and NIR ratios for five independent samples acquired at pH 6 (further details in ESI, section 5, Fig. S6†). Despite the higher variability, all samples predominantly display V_{thres} and NIR ratios oscillating within the range of 1.5–2 V (1.7 ± 0.5) and 15–25 (20 ± 7), respectively.

For its part, the transport of K^+ and ClO_4^- for different channel sizes is shown in Fig. 3 (SEM images and *I–V* curves are available in ESI, sections 1 and 6,† respectively). Bullet-shaped channels of different sizes were created by varying the etching time between 4 and 12 minutes. Considering that the tip is the region where the surface phenomena mostly contribute, the channels will be referred to by their tip sizes (tip and base size values can be found in Table 1). Due to the presence of NIR events, the currents at +3 V evidence smaller values for the channels of 62 and 100 nm in comparison to those observed when the *I–V* curve was conducted in KCl. For instance, in the case of 62 nm-channel, the current at +3 V tends to a value of 1.8 nA which constitutes ~90 times lower than the current value obtained with 0.1 M KCl in the same channel (I^{KCl}/I^{KClO_4} ~90, where I^{KCl} and I^{KClO_4} correspond to the current values obtained for KCl and $KClO_4$, respectively) (Fig. 3(a)). For the case of 100 nm-channel, the current at +3 V tends to a value of ~6 nA which constitutes ~40 times lower than the current value obtained with KCl in the same channel (I^{KCl}/I^{KClO_4} ~40). The situation for the channel of 237 nm, the wider channel, is rather different from the previously exposed since, while an appreciable instability in the currents is evidenced at high V_t, the values of current obtained for $KClO_4$ are similar to those obtained with KCl electrolyte (I^{KCl}/I^{KClO_4} ~1.1). In this case, such a difference can be explained by the inherent differences in the mobilities between ClO_4^- and Cl^-. However, it is worth mentioning that instabilities are obtained in the signal, which indicates that precipitation is still occurring in this channel but in a magnitude that is not enough to produce NIR events or drastic changes in the current.

Table 1 Tip and base sizes for the different bullet-shaped nanochannels shown in Fig. 3

Etching time/min	Tip size/nm	Base size/nm
4	62 ± 20	258 ± 19
6	100 ± 8	357 ± 17
12	237 ± 17	443 ± 14

The trend of the V_{thres} in terms of the number of cycles was analyzed for the different channels (Fig. 3(b)). For the case of the 237 nm channel, the voltage threshold mostly coincides with the maximum voltage applied (3 V) for the different cycles because of the lower effect of nanoprecipitates in the overall response. For its part, the comparison between the 62 nm and 100 nm channels suggests that V_{thres} are required to promote the NIR event as the tip channel diameter decreases.

The analysis of the NIR ratio in terms of the cycle number reveals a constant value of 10 for the smallest channel (Fig. 3(c)). For the channel of 100 nm, the NIR ratio is the highest with a value of ~18 but the instability in the ratio is also the highest. Finally, the low effect of nanoprecipitates in the 237 nm channel determines a NIR ratio of around 1. In line with the results obtained at different pH values, the NIR ratio not only depends on the channel selectivity but instead, arises from an interrelation between selectivity and conductance where a small channel (*e.g.* tip around 62 nm) generates more constant NIR ratio values but with lower magnitudes than a channel of moderated size (*e.g.* tip around of 100 nm).

Therefore, comparing all the cases it is possible to conclude that the trends can be explained by the synergy of two effects: a given amount of precipitates causes a higher occlusion as the channel size diminishes, and in addition, smaller channels generate higher enrichment degrees promoting an increase in the precipitate size. Thus, for the range of sizes studied in this work, the channel diameter diminution favors the appearance of the NIR events. These findings demonstrate

that the possibility to trigger NIR events assisted by salt precipitation is not an exclusive property of sub 10 nm-channel but instead, charged channels with the lowest dimension around 100 nm still evidence these peculiar transport properties.[21,32] This fact constitutes an advantage not only from a fabrication perspective but also facilitates electrochemically recording the phenomenon since the signal magnitude is amplified from dozens of pA to nA. These findings will be comprehensively discussed below for different geometries in Fig. 5.

The hypothesis of salt nanoprecipitation due to the enrichment promoted by nanoconfinement in asymmetrical channels was also tested by comparing the response of channels with different geometries (cylindrical, bullet, and cigar-shaped) under 0.1 M $KClO_4$ at pH 6 (Fig. 4). As was explained in Fig. 1–3, for the case of a bullet-shaped nanochannel, the *I–V* curve by employing 0.1 M $KClO_4$ as supporting electrolyte is characterized by a NIR disruption in the usual ion current rectifying regime (Fig. 4(a)). However, in the case of a cylindrical channel (35 nanometers of diameter), the response is characterized by an ohmic behavior typical of symmetrical systems and the current maintains its stability along the complete scan between ±3 V over 20 cycles, *i.e.* NIR phenomenon is absent (Fig. 4(b)). In addition, for cigar-shaped channels (*i.e.* parabolic profile at both sides of the membrane) with aperture and lumen sizes around 70 nm and 330 nm respectively, the response is characterized by a non-ohmic and non-rectifying behavior in which, similar to cylindrical channels, the current is also maintained over 20 cycles without the appearance of NIR phenomena (Fig. 4(c)).

Given that these channels are obtained using different chemical protocols, it is possible to attribute the absence of the NIR phenomenon to a difference in sizes rather than geometry. It is worth mentioning that the cigar-shaped channel shown in Fig. 4(b) presents similar aperture sizes to those obtained by bullet-shaped channels. In fact, the aperture and inner sizes fall within the range of sizes achieved for bullet-shaped channels created by using etching times of 4 and 6 minutes (see ESI, section 1†). On the other hand, to dispel any doubts about the size effect for cylindrical channels, experiments were conducted with two cylindrical channels of different sizes: the previously mentioned cylindrical nanochannel, with a diameter of 35 nm (shown in Fig. 4(c)), where surface charge governs the ion transport and a micrometric channel with a diameter of 240 nm, *i.e.* within the size range of the base side of the bullet-shaped channel (see ESI, section 7†). In both conditions, the iontronic signal recorded with $KClO_4$ did not display the NIR phenomenon. These results, combined with previous reports from Siwy group,[21] seem to indicate that nanoprecipitation is a phenomenon induced by conical and bullet geometries, that is, nanofluidic devices capable of rectifying the ion current.

To rationalize these results in terms of the ion concentrations inside of the nanostructure computed by numerical simulations, Fig. S9† shows the ion profiles at different V_t for the three geometries. As mentioned earlier, the bullet-shaped nanochannels exhibit ion enrichment at $V_t > 0$ V, which can account for the precipitation of $KClO_4$ and the subsequent abrupt decrease in current. However, in the case of the cylindrical and cigar-shaped geometries, the ion transport profiles differ significantly. In the scenario of the cigar-shaped geometry, the ionic concentration within the nanochannel is significantly lower than those obtained for bullet-shaped geometry, being insufficient to initiate NIR events. In the case of cylindrical channels, cations become enriched, while anions are depleted from the channel at all V_t values. Consequently, the salt concentration does not reach levels above the saturation point.

To reinforce this hypothesis and discard the size effect, a comprehensive analysis of the ion concentration profiles for bullet-shaped, cigar-shaped, and cylindrical channels with different sizes is included in Fig. 5 (further details in ESI, section 8†). As shown in Fig. 5(a), the accumulation degree and the channel volume where the ions are enriched in the bullet-shaped geometry increase as the tip diameter decreases. This trend should favor the appearance of NIR events in

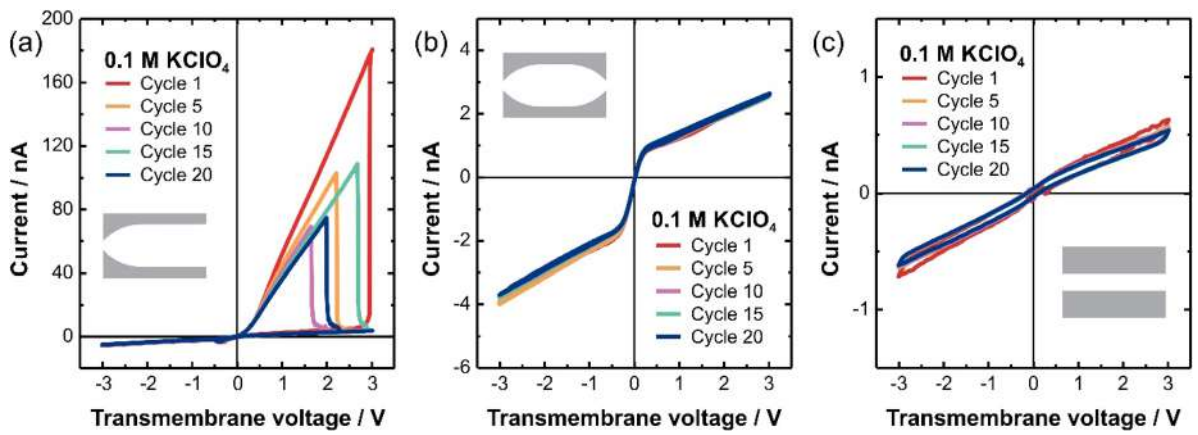

Fig. 4 *I–V* curves obtained for different channel geometries: (a) bullet-shaped (tip: 100 nm; base: 357 nm), (b) cigar-shaped (apertures: 70 nm; inner: 330 nm), and (c) cylindrical channels (35 nm). All the measurements were conducted in 0.1 M $KClO_4$ at pH 6.

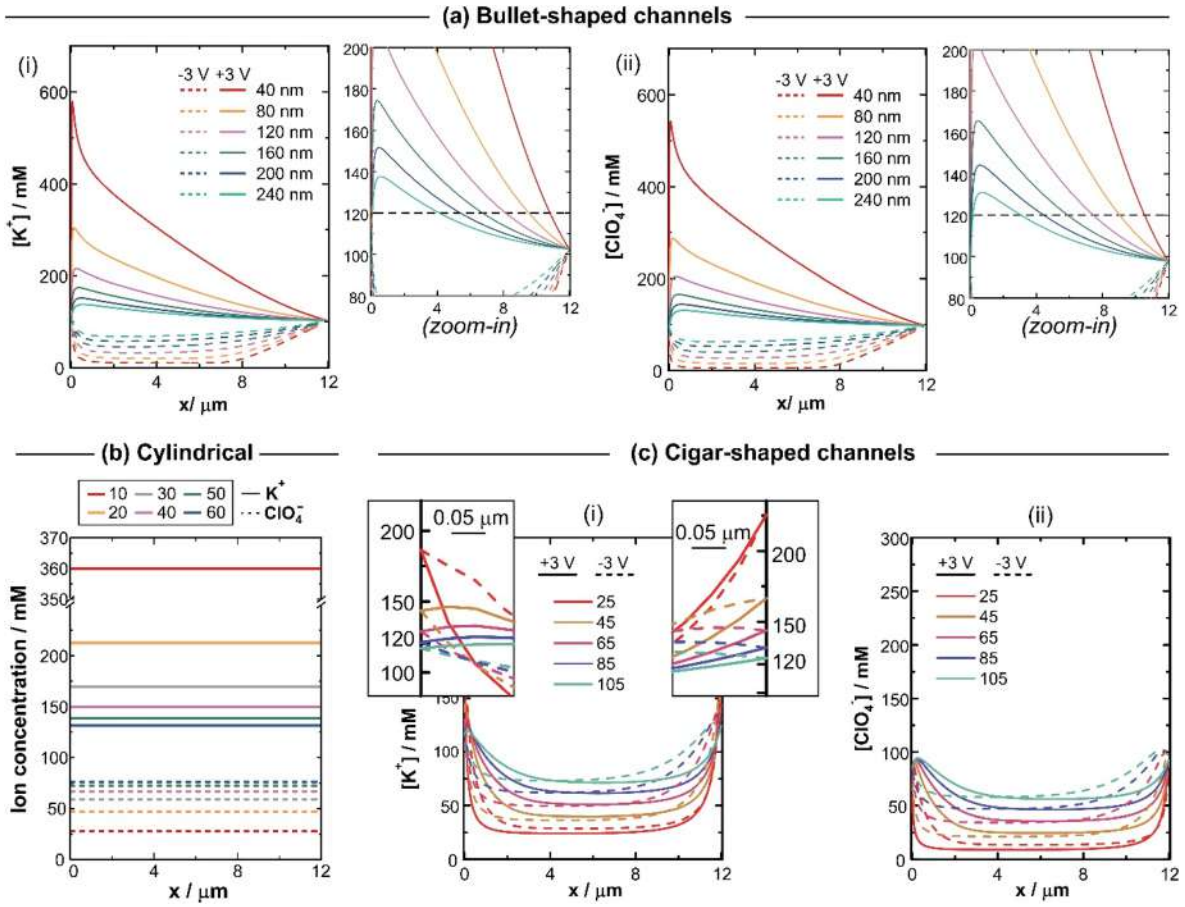

Fig. 5 Ion concentration profiles for (a) bullet-shaped, (b) cylindrical, and (c) cigar-shaped channels with different aperture diameters. In the case of bullet-shaped geometry, the diameter value corresponds to the tip aperture. For figures (a) and (c), full and dash lines correspond to the ion profiles at +3 and −3 V, respectively. Also, figures (i) and (ii) represent the cation and anion concentrations, respectively. For the cylindrical channel, full and dash lines correspond to the cation and anion concentrations at +3 V, respectively. At −3 V, ion profiles are very similar -not shown-. In all the cases, the simulations were conducted considering 0.1 M $KClO_4$ as the supporting electrolyte.

narrow channels, in accordance with the experimental results shown in Fig. 3. However, the results obtained by PNP simulations suggest the possibility of obtaining salt precipitation even in micrometric bullet-shaped channels which agrees with our experimental observations (Fig. S7(f)†). For instance, channels with a tip diameter of 240 nm still display ion concentrations higher than 120 mM through a wide region of the channel (from $x = 0$ to *ca.* $x = 3.5$ μm).

In contrast to the bullet-shaped case, cylindrical channels exhibit cation enrichment and anion depletion in the entire range of diameters studied (Fig. 5(b)). For instance, while the decrease of the aperture diameter for cylindrical channels to values of 10 nm abruptly increments the cation enrichment (~360 mM), the severe anion depletion (~27 mM) maintains the concentration product below the solubility product. Noteworthy, it has been demonstrated that pores with ohmic behavior (as cylindrical ones) might exhibit salt precipitation due to a severe ion concentration polarization.[36] In principle, severe concentration polarization could be promoted in long channels by introducing a highly charged building block with narrow porosity.[50] Finally, the case of cigar channels is more complex (Fig. 5(c)). In all the sizes studied, the cation enrichment is lower than exhibited by bullet-shaped ions and, in addition, anions are mostly depleted. However, it is interesting that the introduction of a little asymmetry in the aperture sizes of cigar-shaped channels rapidly boosts the ion accumulation and, depending on the size, it could be enough for salt precipitation (Fig. S10†). All this PNP-based analysis reinforces the main hypothesis, asymmetrical channels with ion current rectification represent a more favored situation for salt precipitation and, in this case, for promoting NIR events.

The measurement of the transient current at different transmembrane voltage steps may provide more information on the kinetic related to the precipitate formation. As shown in Fig. 6, for V_t steps from −3 V to 1.5 V (gray curve), the transient conductance shows a considerable increment in its value, which is expected due to the switch from a closed state voltage at −3 V to an open state voltage at 1.5 V. However, the situation is quite different when the voltage step is from −3 V to 2.5 or 3 V. Under these steps, the ion transport transitions from a

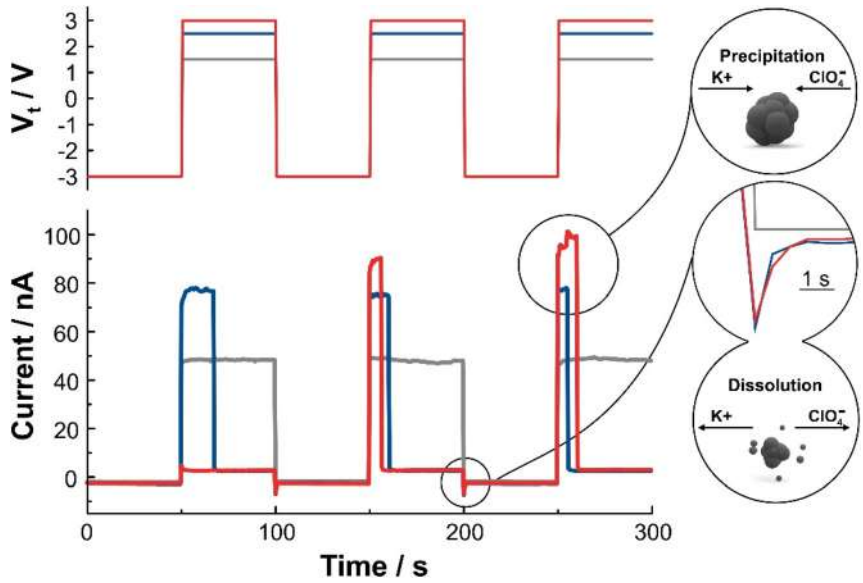

Fig. 6 Transient current (down) for different transmembrane voltage steps (upper) in 0.1 M $KClO_4$ at pH 6.

closed state (−3 V) to an inactivated state (2.5 V or 3 V) and, consequently, the transient current takes small values (<5 nA) during most of the step time.

Beyond this general trend, different issues can be discussed from these results. While current values proper of inactivated state are evident in all the steps from −3 V to 2.5 or 3 V (blue and red curves, respectively), in some cases, the transition from close to inactivated was not an instantaneous event and took <10 seconds. For instance, the first step from −3 V to 3 V (red curve, 50–100 seconds) displayed current values <10 nA which suggests that precipitation blocked very rapidly the channel. On the contrary, the remaining two steps (red curve, 150–200 seconds and 250–300 seconds) firstly evidence high current values that, after a few seconds, decay to values around 4 nA. The time variability in the current drop is in line with the variability obtained for the V_{thres} in the *I–V* curves.

On the other hand, it is very interesting that, if a current blockade is produced in the step from −3 V to 2.5 or 3 V, the following step from 2.5 or 3 V to −3 V displays an instantaneous enhancement in the current (<1 s) and then, it tends to a constant low value (see zoom-in in Fig. 6). As was previously explained, such a small and short-lived increment in the current at negative V_t could be indicative of a partial dissolution of the precipitate and the consequent drain of the released ions.

All these results seem to indicate that the current disruption is not an instantaneous event, however, the kinetic variable is not the most important parameter to observe it. On the contrary, the application of a certain V_t above V_{thres} is the most important operative requirement. *I–V* curves in 0.1 M $KClO_4$ at pH = 6 at different scan rates were also performed to reinforce this statement. As can be seen in Fig. 7(a), *I–V* curves at

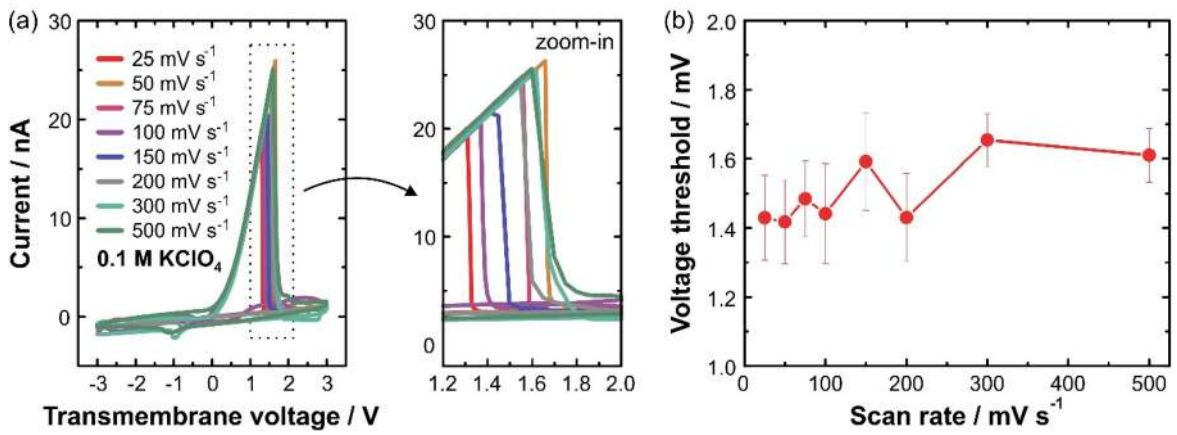

Fig. 7 (a) *I–V* curves in 0.1 M $KClO_4$ at pH 6 obtained under different scan rates. (b) Average voltage threshold (10 cycles) obtained for the different scan rates.

different scan rates present some similarities. In all the cases, the current values obtained in the range 0 V < V_t < 1.5 V take similar values beyond the scan rate. Moreover, V_{thres} does not maintain a strong dependence on the scan rate (Fig. 7(b)). On the contrary, only a small increment of 0.2 V is produced in the voltage threshold when the scan rate is increased from 25 mV s^{-1} to 500 mV s^{-1} which could be related to the high scan rate in comparison to the time needed for the ions to readjust to the electrical potential.

Conclusions

In conclusion, this study provides valuable insight into the transport of salt with moderate solubility through nanochannels. Using bullet-shaped channels and exposing them to $KClO_4$, a monovalent salt with moderate solubility, an iontronic output that combines the typical rectifying behavior with negative incremental resistance phenomena has been evidenced. Notably, this iontronic behavior is not observed in other geometries such as cylindrical or cigar-shaped channels. These results suggest that nanoprecipitation is a phenomenon induced by conical and bullet geometries; *i.e.*, geometries that display ion current rectification. This can be attributed to the ion concentration profiles inside the channel during rectifying regimes.

The influence of conditions such as pH, channel size, and geometry on the rectifying behavior and NIR events has been thoroughly investigated. The results indicate that negative incremental resistance events were only observed at pH values of 6 and 9, *i.e.* when the channel surface was appreciably charged. At acidic pH values, where the surface charge was low, no NIR events were observed. Furthermore, smaller channels with a higher ion enrichment degree are more likely to exhibit NIR events. In contrast, larger channels showed less ion enrichment and were unfavored to exhibit negative incremental resistance events.

In contrast to previous studies, the most extensive use of a method such as cyclic voltammetry to study this phenomenon has allowed to understand how salt precipitation is affected by the different cycle numbers, scan rates, and transmembrane voltage direction. The results suggest that salt precipitates are accumulated cycle by cycle for the first cycles and the phenomenon is not highly influenced by scan rate in the range from 0 to 500 mV s^{-1}. Remarkably, during the backward scan, the appearance of a small NIR event at negative transmembrane voltages seems to indicate partial dissolution of the precipitate formed during the forward scan.

Interestingly, it is possible to draw an analogy between the three distinct conductance regimes observed in this fully abiotic channel and those found in voltage-gated biological ion channels. In biological ion channels, voltage-responsive ion channels have at least two different states depending on membrane potential: closed and open. In some cases, ion channels also have an inactivated state where the channel is closed differently even when the opening stimulus is present. Similarly, in this bioinspired system, ion transport alternates among three stable conductance states: under negative transmembrane voltages, the ion flux is in a low state (closed), while at low and moderate positive transmembrane voltages, the ion flux is favored (open) and conductance takes maximum values. However, further increases in transmembrane voltage disrupt the high conductance branch by promoting a negative differential resistance and giving rise to another low ion flux regime (inactivated).

Conflicts of interest

There are no conflicts to declare.

Acknowledgements

G. L. acknowledges the scholarship from CONICET and the research stay funding provided by DAAD and the GET_INvolved program from GSI. L. M. H.-P. acknowledges the scholarship from CONICET. W. A. M. and O. A. acknowledge the financial support from Universidad Nacional de La Plata (PPID-X867), CONICET (PIP-0370), and ANPCyT (PICT-2017-1523 and PICT2016-1680). O. A. gratefully acknowledges funding from the Georg Förster Award of the Humboldt Foundation. The irradiated PET foils are part of the experiment UMAT, which was performed at the beamline X0 at the GSI Helmhotzzentrum für Schwerionenforschung, Darmstadt (Germany) in the frame of FAIR Phase-0.

References

1 R. MacKinnon, *Angew. Chem., Int. Ed.*, 2004, **43**, 4265–4277.
2 B. Hille, *Ion Channels of Excitable Membranes*, Sinauer Associates Inc., Sunderland, 3rd edn, 2001.
3 M. Tagliazucchi and I. Szleifer, *Mater. Today*, 2015, **18**, 131–142.
4 K. Xiao, L. Wen and L. Jiang, *Small*, 2016, **12**, 2810–2831.
5 G. Pérez-Mitta, W. A. Marmisollé, A. G. Albesa, M. E. Toimil-Molares, C. Trautmann and O. Azzaroni, *Small*, 2018, **14**, 1702131.
6 V. M. Cayón, G. Laucirica, Y. Toum Terrones, M. L. Cortez, G. Pérez-Mitta, J. Shen, C. Hess, M. E. Toimil-Molares, C. Trautmann, W. A. Marmisollé and O. Azzaroni, *Nanoscale*, 2021, **13**, 11232–11241.
7 Y. Toum Terrones, G. Laucirica, V. M. Cayón, G. E. Fenoy, M. L. Cortez, M. E. Toimil-Molares, C. Trautmann, W. A. Mamisollé and O. Azzaroni, *Chem. Commun.*, 2022, **58**, 10166–10169.
8 G. Laucirica, Y. Toum Terrones, V. Cayón, M. L. Cortez, M. E. Toimil-Molares, C. Trautmann, W. Marmisollé and O. Azzaroni, *TrAC, Trends Anal. Chem.*, 2021, **144**, 116425.
9 Q. Ma, Z. Si, Y. Li, D. Wang, X. Wu, P. Gao and F. Xia, *TrAC, Trends Anal. Chem.*, 2019, **115**, 174–186.

10 G. Laucirica, Y. Toum Terrones, M. F. P. Wagner, V. M. Cayón, M. L. Cortez, M. E. Toimil-Molares, C. Trautmann, W. Marmisollé and O. Azzaroni, *Nanoscale*, 2023, **15**, 1782–1793.

11 M.-Y. Wu, Z.-Q. Li, G.-L. Zhu, Z.-Q. Wu, X.-L. Ding, L.-Q. Huang, R.-J. Mo and X.-H. Xia, *ACS Appl. Mater. Interfaces*, 2021, **13**, 32479–32485.

12 J. Li and D. Li, *ACS Appl. Mater. Interfaces*, 2021, **13**, 48208–48218.

13 G. Laucirica, A. G. Albesa, M. E. Toimil-Molares, C. Trautmann, W. A. Marmisollé and O. Azzaroni, *Nano Energy*, 2020, **71**, 104612.

14 Z. Zhang, L. Wen and L. Jiang, *Nat. Rev. Mater.*, 2021, **6**, 622–639.

15 G. Laucirica, M. E. Toimil-Molares, C. Trautmann, W. Marmisollé and O. Azzaroni, *Chem. Sci.*, 2021, **12**, 12874–12910.

16 R. Li, X. Fan, Z. Liu and J. Zhai, *Adv. Mater.*, 2017, **29**, 1702983.

17 R. B. Schoch, J. Han and P. Renaud, *Rev. Mod. Phys.*, 2008, **80**, 839–883.

18 G. Pérez-Mitta, M. E. Toimil-Molares, C. Trautmann, W. A. Marmisollé and O. Azzaroni, *Adv. Mater.*, 2019, **31**, 1901483.

19 Z. S. Siwy, *Adv. Funct. Mater.*, 2006, **16**, 735–746.

20 J. J. Perez-Grau, P. Ramirez, V. Garcia-Morales, J. Cervera, S. Nasir, M. Ali, W. Ensinger and S. Mafe, *ACS Appl. Mater. Interfaces*, 2021, **13**, 54447–54455.

21 M. R. Powell, M. Sullivan, I. Vlassiouk, D. Constantin, O. Sudre, C. C. Martens, R. S. Eisenberg and Z. S. Siwy, *Nat. Nanotechnol.*, 2008, **3**, 51–57.

22 M. Faghih, D. Karnaushenko, Q. A. Besford, C. Becker, R. Ravishankar, D. D. Karnaushenko, G. Cuniberti, A. Fery and O. G. Schmidt, *Adv. Funct. Mater.*, 2022, **32**, 2200233.

23 C.-Y. Lin, P.-H. Wong, P.-H. Wang, Z. S. Siwy and L.-H. Yeh, *ACS Appl. Mater. Interfaces*, 2020, **12**, 3198–3204.

24 L. Luo, D. A. Holden, W.-J. Lan and H. S. White, *ACS Nano*, 2012, **6**, 6507–6514.

25 K. Kobashi, R. Hayakawa, T. Chikyow and Y. Wakayama, *Adv. Electron. Mater.*, 2017, **3**, 1700106.

26 J. Chen, M. A. Reed, A. M. Rawlett and J. M. Tour, *Science*, 1999, **286**, 1550–1552.

27 L. Esaki, *Phys. Rev.*, 1958, **109**, 603–604.

28 E. Alekseev and D. Pavlidis, *Solid-State Electron.*, 2000, **44**, 941–947.

29 S. Bhattacharyya, S. J. Henley, E. Mendoza, L. Gomez-Rojas, J. Allam and S. R. P. Silva, *Nat. Mater.*, 2006, **5**, 19–22.

30 Z. S. Siwy, M. R. Powell, E. Kalman, R. D. Astumian and R. S. Eisenberg, *Nano Lett.*, 2006, **6**, 473–477.

31 Z. S. Siwy, M. R. Powell, A. Petrov, E. Kalman, C. Trautmann and R. S. Eisenberg, *Nano Lett.*, 2006, **6**, 1729–1734.

32 L. Innes, M. R. Powell, I. Vlassiouk, C. Martens and Z. S. Siwy, *J. Phys. Chem. C*, 2010, **114**, 8126–8134.

33 P. Ramirez, J. A. Manzanares, J. Cervera, V. Gomez, M. Ali, I. Pause, W. Ensinger and S. Mafe, *J. Membr. Sci.*, 2018, **563**, 633–642.

34 L. Luo, D. A. Holden and H. S. White, *ACS Nano*, 2014, **8**, 3023–3030.

35 J. Rabinowitz, M. A. Edwards, E. Whittier, K. Jayant and K. L. Shepard, *J. Phys. Chem. A*, 2019, **123**, 8285–8293.

36 E. T. Acar, P. Hinkle and Z. S. Siwy, *J. Phys. Chem. C*, 2018, **122**, 3648–3654.

37 B. Hyland, Z. S. Siwy and C. C. Martens, *J. Phys. Chem. Lett.*, 2015, **6**, 1800–1806.

38 B. Vilozny, P. Actis, R. A. Seger and N. Pourmand, *ACS Nano*, 2011, **5**, 3191–3197.

39 P. Y. Apel and D. Fink, in *Transport Processes in Ion-Irradiated Polymers*, ed. D. Fink, Springer-Verlag Berlin Heidelberg, 2004, pp. 147–202.

40 L. Yang, P. Liu, C. Zhu, Y. Zhao, M. Yuan, X.-Y. Kong, L. Wen and L. Jiang, *Chin. Chem. Lett.*, 2021, **32**, 822–825.

41 P. Ramírez, P. Y. Apel, J. Cervera and S. Mafé, *Nanotechnology*, 2008, **19**, 315707.

42 J. Wang, L. Liu, G. Yan, Y. Li, Y. Gao, Y. Tian and L. Jiang, *ACS Appl. Mater. Interfaces*, 2021, **13**, 14507–14517.

43 M. Karimzadeh, Z. Seifollahi, M. Khatibi and S. N. Ashrafizadeh, *Electrochim. Acta*, 2021, **399**, 139376.

44 P. Ramírez, V. Gómez, J. Cervera, B. Schiedt and S. Mafé, *J. Chem. Phys.*, 2007, **126**, 1–10.

45 D. R. Lide, *CRC Handbook of Chemistry and Physics*, 90th edn, 2010.

46 J. Zheng and M. C. Trudeau, *Handbook of ion channels*, CRC Press, Taylor & Francis Group, 2015.

47 N. Sukomon, C. Fan and C. M. Nimigean, *Annu. Rev. Biophys.*, 2023, **52**, 91–111.

48 G. Yellen, *Q. Rev. Biophys.*, 1998, **31**, 239–295.

49 C. M. Armstrong and F. Bezanilla, *J. Gen. Physiol.*, 1977, **70**, 567–590.

50 G. Laucirica, J. A. Allegretto, M. F. Wagner, M. E. Toimil-Molares, C. Trautmann, M. Rafti, W. Marmisollé and O. Azzaroni, *Adv. Mater.*, 2022, 2207339.